Journal of Power Sources 255 (2014) 335–340

Contents lists available at ScienceDirect

Journal of Power Sources

journal homepage: www.elsevier.com/locate/jpowsour

Short communication

Electrospun nanofiber of hybrid manganese oxides for supercapacitor: Relevance to mixed inorganic interfaces

Eunhee Lee, Taemin Lee, Byeong-Su Kim*

Interdisciplinary School of Green Energy and Department of Chemistry, Ulsan National Institute of Science and Technology (UNIST), Ulsan 689-798, Republic of Korea

HIGHLIGHTS

- 3-Dimensional MnO_x nanofiber was formed by electrospinning.
- Upon calcination at different temperatures, MnO_x NFs became variable composition of Mn_3O_4 to Mn_2O_3.
- This study examined the supercapacitor performance depending on the phases of MnO_x.
- We found that mixed phase exhibited a higher capacity than that of respective single phase.
- The high specific capacitance was attributed to 3D structure and the reduced interfacial resistance.

ARTICLE INFO

Article history:
Received 3 December 2013
Received in revised form
5 January 2014
Accepted 6 January 2014
Available online 15 January 2014

Keywords:
Electrospun nanofiber
Manganese oxides
Mixed phase
Supercapacitor
Three-dimensional (3D) electrode

ABSTRACT

We prepare electrospun nanofibers (NFs) from a poly(N-vinylpyrrolidone)/manganese (II) acetate composite by electrospinning for application in supercapacitors. As-spun hybrid NFs are calcined at different temperatures to remove the polymer matrix, resulting in inorganic MnO_x NFs of variable compositional ratios of Mn_3O_4 to Mn_2O_3. Interestingly, the sample of MnO_x NFs that is calcined at 500 °C exhibits the highest electrochemical performance, reaching a high specific capacitance of 360.7 F g^{-1} at a current density of 1 A g^{-1}. This remarkable performance is attributed to the unique three-dimensional morphology and the reduced interfacial resistance of the mixed-phase MnO_x NFs within the matrix electrode and the electrolyte.

1. Introduction

Due to the exhaustion of natural resources and associated environmental issues as well as the increasing demand of energy for future portable devices and electric vehicles, there has been an intense interest in alternative energy conversion and storage systems with high efficiency, low cost, and environmental benignity [1–3]. Among many energy storage devices, electrochemical capacitors, also known as supercapacitors, have attracted considerable attention because of their high power density, fast charge–discharge rate, long cycle life, wide thermal operating range, and low maintenance cost. Therefore, the performance of electrochemical capacitors is complementary to those of secondary batteries and fuel cells [4–6].

Supercapacitors are generally classified into two types depending on their charge storage mechanism and the active materials used. Electric double-layer capacitors store electrical charges at the interface of a porous, carbon-based electrode and an electrolyte based on the non-Faradaic reaction [4,7,8]. On the other hand, pseudocapacitors utilize the Faradaic reaction of redox-active materials such as conducting polymers and metal oxides [4,9–11]. In particular, transition metal oxides that exhibit pseudocapacitive behavior, such as RuO_2 [12–14], MnO_x, NiO [15,16], CoO [17], and Fe_3O_4 [18], have been proposed as promising electrode materials for supercapacitors because of their high capacitance and good cycling stability. Among the above oxides, manganese oxide (MnO_x) is clearly noteworthy, displaying fine specific capacitance (200–600 F g^{-1}) and reversible charge–discharge feature with its natural abundance and low cost [6,19–22]. Despite these favorable features of MnO_x, its poor electric conductivity and stability often cause unsatisfactory performance in supercapacitors. In addition, various oxidation states of MnO_x result in a range of different crystalline

* Corresponding author. Tel.: +82 52 217 2923; fax: +82 52 217 2019.
E-mail addresses: bskim19@gmail.com, bskim19@unist.ac.kr (B.-S. Kim).

0378-7753/$ – see front matter © 2014 Elsevier B.V. All rights reserved.
http://dx.doi.org/10.1016/j.jpowsour.2014.01.011

phases with potentially different electrochemical behaviors. However, the relationship between phase structure and electrochemical properties of MnO_x has not been fully studied.

In order to improve supercapacitor performance, several approaches have been proposed, including developing new materials by deposition of electroactive metallic nanoparticles and conducting polymers, and creating new electrode structures [4,22–24]. As a representative approach, three-dimensional (3D), porous electrodes are known to exhibit superior capacitance because of increased specific surface area and enhanced access of electrolytes to the surface of the electrodes. In this regard, electrospinning can form porous, 3D electrodes from continuous, 1D nanofibers (NFs) of various materials [25–28]. Furthermore, electrospinning not only fabricates polymer and inorganic fibers with various dimensions, but also produces unique fiber structures such as hollow, core–shell, or porous structure [29–31].

In this report, we describe the fabrication of porous, 3D electrodes composed of MnO_x NFs by electrospinning for application in supercapacitors (Scheme 1). Specifically, a polymer matrix of poly(N-vinylpyrrolidone) (PVP) mixed with manganese (II) acetate ($Mn(CH_3COO)_2$ or $Mn(OAc)_2$) was employed to form continuous, 3D NFs of controlled dimensions. Upon calcination at different temperatures (400, 500, 600, and 700 °C), these NFs were transformed into hybrid MnO_x NFs with a varying degree of mixed phase of Mn_3O_4 and Mn_2O_3 in varying ratios. Interestingly, the relative composition of each phase was demonstrated to have a considerable influence on the supercapacitor performance by a series of electrochemical characterization measurements. For example, we confirmed that a mixed phase of Mn_2O_3 and Mn_3O_4 delivered a higher capacitance (360.7 F g^{-1}) than either of its individual material oxide taken individually, arising from the unique 3D morphology and the reduced interfacial resistance of the mixed phase within the matrix electrode and the electrolyte.

2. Experimental

2.1. Preparation of electrospun MnO_x NFs

Poly(N-vinyl pyrrolidone) (PVP) solution was prepared by dissolving PVP powder (M_w 1,300,000 g mol^{-1}) in deionized water (20 wt%). Then, $Mn(OAc)_2$/PVP solution was prepared by dissolving manganese acetate (20 wt%) in PVP solution. This solution was stirred for at least one day in order to obtain homogeneously distributed solutions. The solution obtained was injected from a syringe and syringe was fixed in syringe pump. The size of the needle in the electrospinning was 25 G, and the needle was connected to high-voltage power supply. The flow rate of the syringe pump was fixed at 10 μl min^{-1}, and the distance between the needle and collector was 10 cm and the applied voltage was 25 kV. The electrospun $Mn(OAc)_2$/PVP NFs were annealed at different temperatures (400, 500, 600 and 700 °C) to remove the polymer matrix and result in the MnO_x NFs.

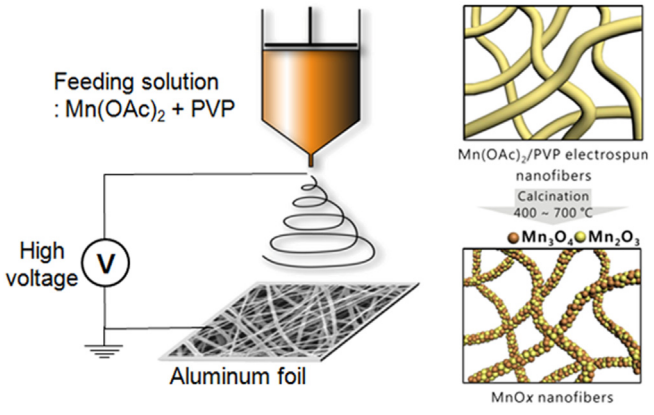

Scheme 1. Schematic representation for the fabrication of the electrospun fiber and subsequent calcination process for hybrid MnO_x NF supercapacitors.

2.2. Structural characterizations

The morphology and fiber diameter of the prepared MnO_x NFs were investigated using a field emission scanning electron microscopy (FESEM, FEI, Nanonova 230) and transmission electron microscopy (TEM, JEOL JEM-2100 accelerating voltage of 200 kV, Gatan CCD camera). X-ray diffraction (XRD) measurements were employed by a high-power X-ray diffractometer (Rigaku Co., D/MAZX 2500V/PC) from 10° to 80°.

2.3. Electrochemical characterization

Electrochemical performance of the electrospun MnO_x NFs were carried out with a standard three-electrode test cell with 0.5 M Na_2SO_4 aqueous solution as electrolyte. Platinum wire and Ag/AgCl were used as a counter and reference electrode, respectively. The characterization of the electrochemical performance for the MnO_x electrode was conducted using a VMP3 electrochemical potentiostat (BioLogic Inc.). Cyclic voltammograms (CVs) and the galvanostatic charge–discharge test were carried out with a potential window from −0.2 to 0.8 V versus Ag/AgCl in 0.50 M Na_2SO_4 electrolyte with scan rates from 5 to 200 mV s^{-1} and a current density of 1 A g^{-1}. In order to internal resistance of MnO_x electrode, measurement of electrochemical impedance was performed in frequency range of 100 kHz–100 MHz.

3. Results and discussion

3.1. Characterization of electrospun MnO_x NFs

Initially, $Mn(OAc)_2$/PVP NFs were successfully fabricated by electrospinning using the procedures outlined in the experimental section. Fig. 1 shows the SEM images and diameter distribution of the as-spun $Mn(OAc)_2$/PVP NFs and the MnO_x NFs formed after calcination at temperatures from 400 to 700 °C. As shown in Fig. 1a, as-spun $Mn(OAc)_2$/PVP NFs were randomly oriented in a continuous, 3D, porous internal structure. The range of NF diameters in the sample was relatively narrow, and no beads were formed. The polymeric component (PVP) was completely degraded at ~400 °C in air, as determined by thermogravimetric analysis (TGA). Accordingly, the as-spun $Mn(OAc)_2$/PVP NFs were calcined above 400 °C in air (Fig. S1 in Supporting information). After calcination at different temperatures, the 3D porous structure was retained without significant structural deformation. However, the diameter of MnO_x NFs decreased after calcination due to the removal of the PVP matrix and the crystallization of MnO_x; for example, the average diameter of as-spun fiber decreased from 135 ± 18 nm to 72.3 ± 14.3 nm (400 °C), 64.2 ± 12.6 nm (500 °C), 52.7 ± 8.9 nm (600 °C) and 54.5 ± 6.9 nm (700 °C), respectively.

Various forms of manganese oxide such as α-MnO_2, δ-MnO_2, λ-MnO_2, Mn_2O_3, and Mn_3O_4 are known to exist depending on the conditions of annealing [32]. We further characterized the phase composition of MnO_x NFs after calcination by X-ray diffraction (XRD) (Fig. 2). The XRD patterns of MnO_x fibers calcined at different temperatures corresponded to either Mn_3O_4 (JCPDS 024-0734) or Mn_2O_3 (JCPDS 073-1826), or a combination of both. The NFs calcined at 400 °C adopted the tetragonal Mn_3O_4 phase exclusively (Fig. 2a). Above 400 °C, Mn_3O_4 transformed into the more oxidized

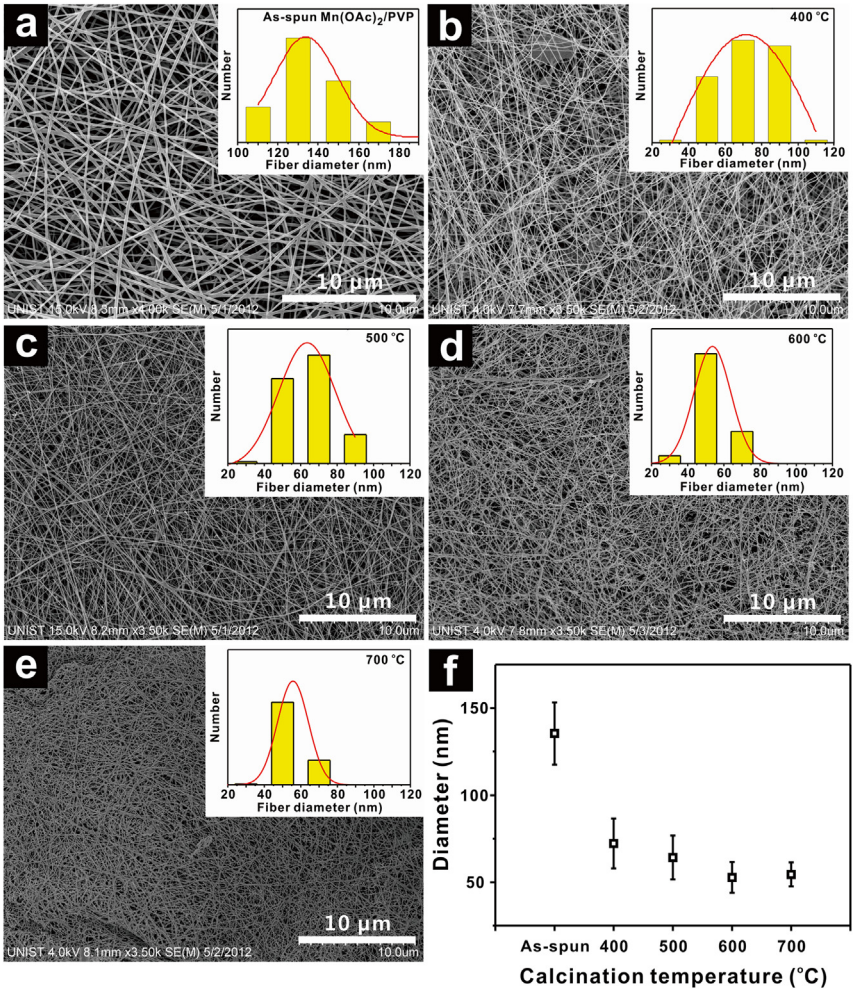

Fig. 1. (a) SEM images of as-spun $Mn(OAc)_2$/PVP NFs. (b–e) SEM images of MnO_x NFs produced from the $Mn(OAc)_2$/PVP NFs by calcination at (b) 400, (c) 500, (d) 600, and (e) 700 °C for 2 h in air. The inset graphs show the diameter distribution of each NF. (f) Plot of average diameter obtained from more than 50 individual SEM images as a function of the calcination temperature. The standard deviations are given as error bar.

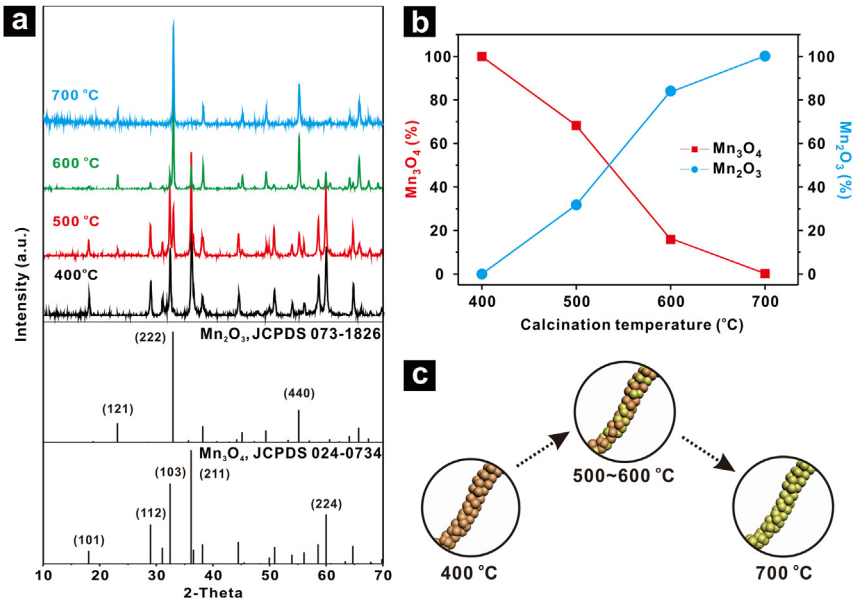

Fig. 2. (a) XRD patterns of the MnO_x NFs after calcination at 400–700 °C compared to the patterns of neat Mn_3O_4 and Mn_2O_3. (b) Plot of relative phase compositions of MnO_x NFs as a function of the calcination temperature. (c) Schematic representation of the phase changes of MnO_x NFs as a function of the temperature.

Mn_2O_3 as the calcination temperature increased, giving mixed-phase nanofibers (MnO_x NFs) (Fig. 2b and c). We correlated the compositional ratio between Mn_3O_4 to Mn_2O_3 on the basis of the main XRD peak intensity ratio, assuming there is no other crystalline phases of MnO_x NFs. Specifically, the ratio of Mn_3O_4 to Mn_2O_3 decreased from 100:0 (400 °C) to 68:32 and 18:82 at 500 and 600 °C, respectively, and at 700 °C, the initial Mn_3O_4 phase transformed into Mn_2O_3 completely.

We further investigated the internal structure of the sample annealed at 500 °C by transmission electron microscopy (TEM) and electron mapping by energy-dispersive spectroscopy (EDS) to confirm the existence of both Mn_3O_4 and Mn_2O_3 phases (Fig. 3). The hybrid MnO_x NFs were composed of granular nanoparticles with diameters of 61 ± 12 nm that were connected along the framework of the NFs. In addition, the high-resolution TEM image revealed that MnO_x NFs were crystalline. The crystalline lattice fringes of 0.24 and 0.49 nm corresponded to the primary reflection of the (211) and (101) peak of Mn_3O_4, respectively. Furthermore, the electron diffraction pattern of a selected area of MnO_x also exhibited a lattice fringe of 0.384 nm, which is associated with the (121) peak of Mn_2O_3 (Fig. 3b). We also confirmed that Mn and O were distributed homogeneously within the electrospun MnO_x NFs by EDS (Fig. 3c). Overall, the high-resolution TEM image and the electron diffraction pattern confirmed the presence of mixed phase of Mn_3O_4 and Mn_2O_3 in the MnO_x NFs calcined at 500 °C, in good agreement with the result of XRD.

3.2. Evaluation of capacitive performance

We investigated the electrochemical properties of hybrid MnO_x NFs calcined at different temperatures by cyclic voltammetry (CV) measurements. All CV data were measured in 0.5 M Na_2SO_4 electrolytes at potential intervals from −0.2 to 0.8 V with platinum wire and Ag/AgCl as a counter and reference electrode, respectively (Fig. 4). All MnO_x NF electrodes displayed the typical broad redox peaks in the potential range investigated. In particular, the CV curves of MnO_x annealed at 400 and 500 °C clearly showed the redox transitions of MnO_x characteristic pseudocapacitive behavior. The specific capacitance values obtained from CV ($C_{sp,CV}$) were determined to be 140.1, 214.7, 69.0, and 46.3 F g^{-1} for electrodes prepared from MnO_x NF calcined at 400, 500, 600, and 700 °C, respectively, at a scan rate of 10 mV s^{-1}. Interestingly, among all electrodes prepared from MnO_x NFs, the one calcined at 500 °C exhibited the highest $C_{sp,CV}$ value. In addition, the linear response of the capacitive current to changes in the potential scan rate revealed that the redox behavior of the system was highly reversible (**inset** in Fig. 4b). Therefore, the capacitance of each electrode strongly depended on the compositional ratio of Mn_2O_3 and Mn_3O_4; for example, Mn_3O_4-rich phases (NFs calcined at 400 and 500 °C) exhibited higher $C_{sp,CV}$ and $C_{sp,G}$ than Mn_2O_3-rich phases (NFs calcined at 600 and 700 °C). Also, the sample annealed at 500 °C with a mixed phase of Mn_2O_3 and Mn_3O_4 showed a higher $C_{sp,CV}$ and $C_{sp,G}$ than that of pure Mn_3O_4 sample annealed at 400 °C.

We further evaluated the supercapacitor performance of all MnO_x electrodes by the galvanostatic charge–discharge test under an identical three-electrode system. The non-linear charge–discharge curves are characteristics for the pseudocapacitive behavior (Fig. 4d). The specific capacitance based on the galvanostat ($C_{sp,G}$) is calculated by the following equation:

$$C_{sp,G}\left(\mathrm{F\,g^{-1}}\right) = (i \times \Delta t)/\Delta E \times m$$

where i is the discharge current (A), Δt is discharge time (s), ΔE is the voltage difference (V), and m is the active mass of electrode (g). The galvanostatic test-based specific capacitance ($C_{sp,G}$) of the MnO_x electrodes annealed at 500 °C was calculated to be 367 F g^{-1} at a current density of 1 A g^{-1}, the highest among all samples. The trends of the galvanostat and CV measurements agree well with each other, even though the values for the latter are higher.

The value obtained from galvanostatic measurements is comparable to the value (highest capacitance of 230.5 F g^{-1} at a scan rate of 25 mV s^{-1} at calcination temperature of 300 °C) published in a recent study by Lin et al., in which the supercapacitor properties of different phases of MnO_x film coated by a sol–gel process and annealed at 250–400 °C were evaluated [33]. In contrast, the MnO_x NFs prepared in this study exhibited considerably higher capacitance than the MnO_x film prepared by a sol–gel process owing to

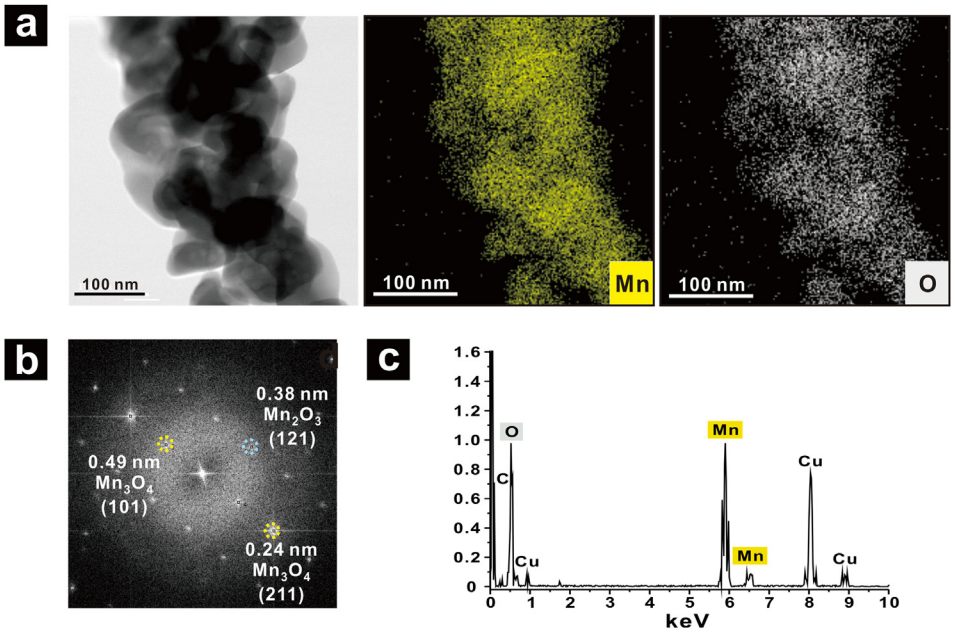

Fig. 3. (a) TEM image and EDS mapping of Mn and O in MnO_x NF calcined at 500 °C. (b) Electron diffraction pattern and (c) map sum spectrum of MnO_x NFs calcined at 500 °C.

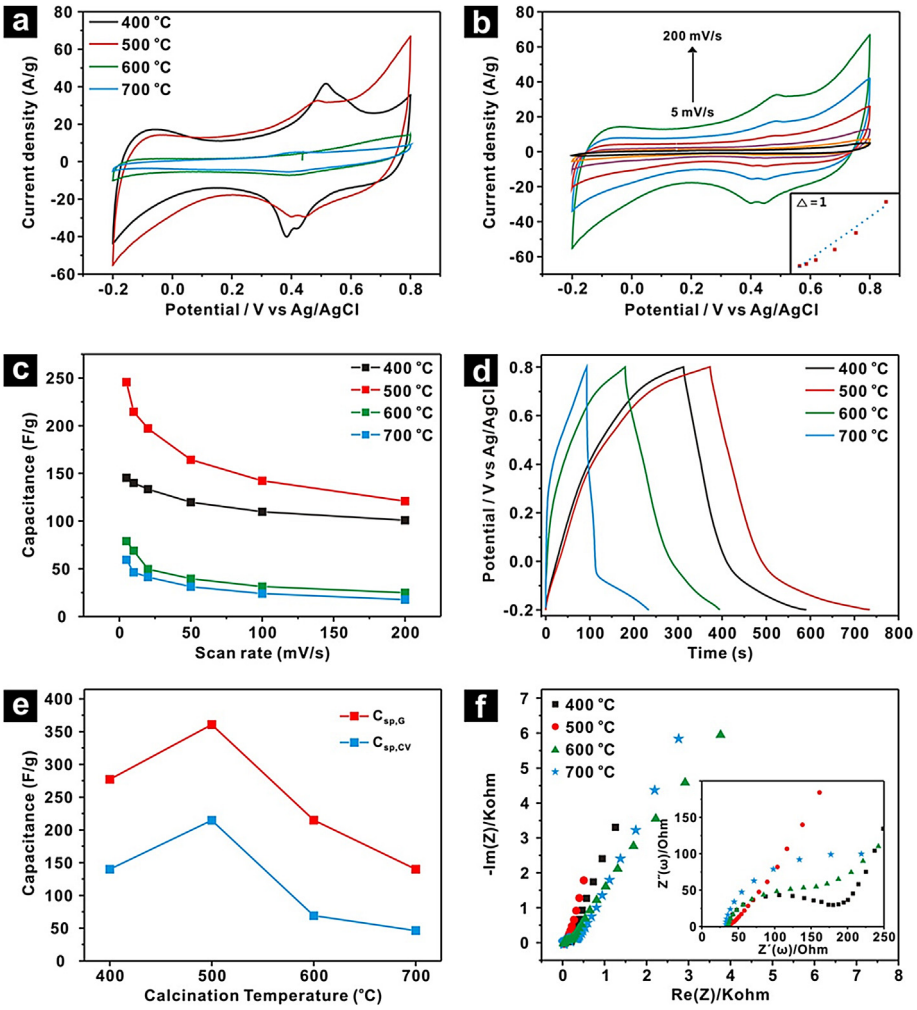

Fig. 4. (a) Cyclic voltammetry (CV) curves at a scan rate of 200 mV s^{-1} of all MnO_x NFs calcined at the specified temperatures. (b) A plot of the current densities of the MnO_x NFs calcined at 500 °C at scan rates from 5 to 200 mV s^{-1}. (c) Dependence of the capacitance on the calcination temperature. (d) Galvanostatic charge–discharge curves of MnO_x NFs calcined at the specified temperatures at a current density of 1 A g^{-1}. (e) $C_{sp,CV}$ and $C_{sp,G}$ of electrodes prepared from MnO_x as a function of the calcination temperature. (f) Nyquist plots of the electrochemical impedance spectroscopy (EIS) for the electrospun MnO_x electrodes as a function of the calcination temperature. Inset represents the high-frequency region.

their unique 3D internal structures. Our study also suggested that electrospinning permits the creation of 3D electrodes that are characterized by both increased surface area and efficient and fast ion transport between the electrode and electrolyte, thus enhancing the electrochemical properties of the supercapacitor.

The kinetics and interfacial resistance that are critical in the evaluation of the electrochemical reactions can be studied by electrochemical impedance spectroscopy (EIS). We thus investigated the charge transfer resistance (R_{CT}) of all four MnO_x NF electrodes in order to elucidate whether capacity was significantly dependent on the phase changes in MnO_x. We determined that the R_{CT} value of MnO_x electrode annealed at 500 °C (6 Ω) was far lower than those of the other three samples (118 Ω, 125 Ω, and 268 Ω at 400 °C, 600 °C, and 700 °C, respectively). This result indicates that the mixed phase of Mn_3O_4 and Mn_2O_3 exhibits a lower charge-transfer resistance, which accounts for the improved electrochemical performance of the supercapacitors. In addition to the above observation, we argue that the enhanced supercapacitive performance stems from the balance between the conductivity and capacitance of two different phases of MnO_x NFs, such as Mn_3O_4 and Mn_2O_3. It is known that the conductivity of the Mn_2O_3 is relatively lower than that of Mn_3O_4, while the capacitance of the former is comparatively higher than that of latter [19,34–37]. Thus, the fine balance between the conductivity and capacitance of two different phases of MnO_x NFs may result in the enhanced capacitance of the mixed phase MnO_x NFs [38]. Although further in-depth analyses of the role of different phases within the electrospun fiber matrix of MnO_x electrode are still required, the results presented here highlight the potential of electrospinning for producing electroactive 3D electrodes.

4. Conclusion

We prepared MnO_x NFs by electrospinning. As-produced NFs were calcined at temperatures from 400 to 700 °C to remove the polymer matrix of poly(N-vinylpyrrolidone) that was used during the electrospinning. MnO_x NFs with varying composition of Mn_2O_3 and Mn_3O_4 were formed after the calcination. XRD measurements suggested that the phase of the as-prepared, amorphous MnO_x NFs changed from Mn_3O_4 to Mn_2O_3, when the calcination temperature increased from 400 to 700 °C. We found that the MnO_x NF sample annealed at 500 °C displayed a capacitance value of 360.7 F g^{-1} at a current density of 1 A g^{-1} (the highest among all samples). This NF sample contained a mixed phase of Mn_2O_3 and Mn_3O_4. Further

electrochemical studies revealed that a unique 3D morphology coupled with a reduced charge transfer resistance of the mixed phase of Mn_2O_3 and Mn_3O_4 contributed to the enhanced supercapacitor performance of MnO_x NFs. We anticipate that this technique will address critical questions regarding the fundamental relationship between structure and energy storage properties as well as bridge the performance gap between batteries and capacitors in the future.

Acknowledgment

This research is supported by the National Research Foundation of Korea (NRF) grant (2012R1A1A2040782).

Appendix A. Supplementary data

Supplementary data related to this article can be found at http://dx.doi.org/10.1016/j.jpowsour.2014.01.011.

References

[1] A.S. Arico, P. Bruce, B. Scrosati, J.M. Tarascon, W. Van Schalkwijk, Nat. Mater. 4 (2005) 366–377.
[2] B.E. Conway, J. Electrochem. Soc. 138 (1991) 1539–1548.
[3] B. Dunn, H. Kamath, J.M. Tarascon, Science 334 (2011) 928–935.
[4] P. Simon, Y. Gogotsi, Nat. Mater. 7 (2008) 845–854.
[5] R. Liu, J. Duay, S.B. Lee, Chem. Commun. 47 (2011) 1384–1404.
[6] J.W. Lee, A.S. Hall, J.D. Kim, T.E. Mallouk, Chem. Mater. 24 (2012) 1158–1164.
[7] S. Bose, T. Kuila, A.K. Mishra, R. Rajasekar, N.H. Kim, J.H. Lee, J. Mater. Chem. 22 (2012) 767–784.
[8] L.L. Zhang, X.S. Zhao, Chem. Soc. Rev. 38 (2009) 2520–2531.
[9] X. Zhao, B.M. Sanchez, P.J. Dobson, P.S. Grant, Nanoscale 3 (2011) 839–855.
[10] H. Jiang, J. Ma, C.Z. Li, Adv. Mater. 24 (2012) 4197–4202.
[11] C.D. Lokhande, D.P. Dubal, O.S. Joo, Curr. Appl. Phys. 11 (2011) 255–270.
[12] C.C. Hu, K.H. Chang, M.C. Lin, Y.T. Wu, Nano Lett. 6 (2006) 2690–2695.
[13] Z.S. Wu, D.W. Wang, W. Ren, J. Zhao, G. Zhou, F. Li, H.M. Cheng, Adv. Funct. Mater. 20 (2010) 3595–3602.
[14] E. Seo, T. Lee, K.T. Lee, H.K. Song, B.S. Kim, J. Mater. Chem. 22 (2012) 11598–11604.
[15] J.W. Lee, T. Ahn, J.H. Kim, J.M. Ko, J.D. Kim, Electrochim. Acta 56 (2011) 4849–4857.
[16] J. Cheng, G.P. Cao, Y.S. Yang, J. Power Sources 159 (2006) 734–741.
[17] W.J. Zhou, J. Zhang, T. Xue, D.D. Zhao, H.L. Li, J. Mater. Chem. 18 (2008) 905–910.
[18] X. Du, C.Y. Wang, M.M. Chen, Y. Jiao, J. Wang, J. Phys. Chem. C. 113 (2009) 2643–2646.
[19] J.K. Chang, Y.L. Chen, W.T. Tsai, J. Power Sources 135 (2004) 344–353.
[20] N. Nagarajan, H. Humadi, I. Zhitomirsky, Electrochim. Acta 51 (2006) 3039–3045.
[21] X. Zhao, L.L. Zhang, S. Murali, M.D. Stoller, Q.H. Zhang, Y.W. Zhu, R.S. Ruoff, ACS Nano 6 (2012) 5404–5412.
[22] W. Chen, R.B. Rakhi, H.N. Alshareef, J. Mater. Chem. 22 (2012) 14394–14402.
[23] M.J. Zhi, C.C. Xiang, J.T. Li, M. Li, N.Q. Wu, Nanoscale 5 (2013) 72–88.
[24] T. Lee, T. Yun, B. Park, B. Sharma, H.K. Song, B.S. Kim, J. Mater. Chem. 22 (2012) 21092–21099.
[25] V. Thavasi, G. Singh, S. Ramakrishna, Energy Environ. Sci. 1 (2008) 205–221.
[26] S. Cavaliere, S. Subianto, I. Savych, D.J. Jones, J. Roziere, Energy Environ. Sci. 4 (2011) 4761–4785.
[27] Y.W. Ju, G.R. Choi, H.R. Jung, C. Kim, K.S. Yang, W.J. Lee, J. Electrochem. Soc. 154 (2007) A192–A197.
[28] S.H. Choi, T.S. Hyun, H. Lee, S.Y. Jang, S.G. Oh, I.D. Kim, Electrochem. Solid-State Lett. 13 (2010) A65–A68.
[29] A. Greiner, J.H. Wendorff, Angew. Chem. Int. Ed. 46 (2007) 5670–5703.
[30] D. Li, Y.N. Xia, Nano Lett. 4 (2004) 933–938.
[31] J.S. Lee, O.S. Kwon, S.J. Park, E.Y. Park, S.A. You, H. Yoon, J. Jang, ACS Nano 5 (2011) 7992–8001.
[32] D.M. Robinson, Y.B. Go, M. Mui, G. Gardner, Z.J. Zhang, D. Mastrogiovanni, E. Garfunkel, J. Li, M. Greenblatt, G.C. Dismukes, J. Am. Chem. Soc. 135 (2013) 3494–3501.
[33] C.K. Lin, K.H. Chuang, C.Y. Lin, C.Y. Tsay, C.Y. Chen, Surf. Coat. Technol. 202 (2007) 1272–1276.
[34] E.M. Logothetis, K. Park, Solid State Commun. 16 (1975) 909–912.
[35] J.W. Long, D. Belanger, T. Brousse, W. Sugimoto, M.B. Sassin, O. Crosnier, MRS Bull. 36 (2011) 513–522.
[36] P.H. Klose, J. Electrochem. Soc. 117 (1970) 854–858.
[37] T. Nathan, M. Cloke, S.R.S. Prabaharan, J. Nanomater. 2008 (2008) 8.
[38] M.K. Song, S. Cheng, H.Y. Chen, W.T. Qin, K.W. Nam, S.C. Xu, X.Q. Yang, A. Bongiorno, J. Lee, J.M. Bai, T.A. Tyson, J. Cho, M.L. Liu, Nano Lett. 12 (2012) 3483–3490.